Nonlinear Aerodynamics of Bodies in Coning Motion

LEWIS B. SCHIFF*
NASA Ames Research Center, Moffett Field, Calif.

A numerical method for computing the nonlinear inviscid flowfield surrounding a body performing coning motion is described. The method permits accurate computation of the aerodynamic moment due to one of the four motions characterizing an arbitrary nonplanar motion. Results of computations for a slender circular cone in coning motion are presented, and show good agreement with experiment for angles of attack up to twice the cone half-angle. The computational results display significant departure of the side moment from the linear theory value with increasing angle of attack, but agree well with experimental measurements. This indicates that the initial nonlinear behavior of the aerodynamic moment is determined primarily by the inviscid flow.

Nomenclature

C_Y = side-force coefficient in the aerodynamic axis system (along y), 2(side force)/$\rho_0 V^2 S$
C_Z = normal-force coefficient in the aerodynamic axis system (along z), 2(normal force)/$\rho_0 V^2 S$
$\hat{C}_Y, \hat{C}_Z$ = side-force and normal-force coefficients in the body-axis system; along y_B, z_B, respectively
C_l = rolling-moment coefficient in the aerodynamic axis system (along x_B), $2\bar{L}/\rho_0 V^2 Sl$
C_m = pitching-moment coefficient in the aerodynamic axis system (along y), $2\bar{M}/\rho_0 V^2 Sl$
C_n = side-moment coefficient in the aerodynamic axis system (along z), $2\bar{N}/\rho_0 V^2 Sl$
$\hat{C}_l, \hat{C}_m, \hat{C}_n$ = rolling, pitching, and yawing-moment coefficients in the body-axis system; along x_B, y_B, z_B, respectively
h_0 = total enthalpy
$\bar{L}, \bar{M}, \bar{N}$ = moment components along the x_B, y, z aerodynamic axes, respectively
l_{cg} = distance from center of gravity to nose of body, $(-s_{tip})$
l = reference length [body length, $(s_{final} - s_{tip})$]
p = pressure
p_B, q_B, r_B = components along the x_B, y_B, z_B axes, respectively, of the total angular velocity of the body axes relative to inertial space
q, r = components of the total angular velocity along the y, z aerodynamic axes, respectively, Eq. (2)
S = reference area (body base area)
s, τ, θ = computational axes, origin at center of gravity, s positive in the negative x_B direction, τ and θ polar coordinates in planes normal to s, Fig. 1
t = time
u_B, v_B, w_B = components of flight velocity along x_B, y_B, z_B axes, respectively, Fig. 1
u, v, w = components of local flow velocity in the s, τ, θ directions, respectively
V = flight velocity
x_B, y_B, z_B = body-fixed axes, origin at center of gravity, x_B coincident with a longitudinal axis of the body, Fig. 1
x_B, y, z = aerodynamic axes, origin at center of gravity, x_B, z in the plane of the resultant angle of attack, y in the crossflow plane normal to the resultant angle-of-attack plane, Fig. 1
α, β = angle of attack and sideslip in body axes, respectively, Eq. (3)
$\hat{\alpha}$ = angle-of-attack parameter in body-axis system, w_B/V
$\hat{\beta}$ = angle-of-sideslip parameter in body-axis system, v_B/V
γ = dimensionless axial component of flight velocity (along x_B), Fig. 1 and Eq. (1)
$\bar{\gamma}$ = ratio of specific heats
δ = magnitude of the dimensionless crossflow flight velocity in the aerodynamic axis system, Fig. 1 and Eq. (1)
η = transformed circumferential independent coordinate, Eq. (10)
μ = transformed radial independent coordinate, Eq. (10)
ρ = local flow mass density
ρ_0 = atmospheric mass density
σ = resultant angle of attack defined by x_B axis and flight velocity vector, Fig. 1
Φ = centrifugal potential, Eq. (9)
$\dot{\phi}$ = coning rate of x_B axis about the flight velocity vector, Fig. 1 (for body in coning motion, total angular velocity of body-fixed axes with respect to inertial space)
ψ = angular inclination of the z_B axis from the z axis in the crossflow plane, Fig. 1
$\omega_1, \omega_2, \omega_3$ = components of total angular velocity in the s, τ, θ directions, respectively
$(\dot{})$ = $(d/dt)(\ )$

Introduction

A PREVIOUS study[1] has shown the nonlinear aerodynamic moment acting on a body performing large-amplitude nonplanar motions to be compounded of the moments acting on the body performing four characteristic motions: steady angle-of-attack, damping-in-pitch, damping-in-roll, and coning motion. Coning motion, where the nose of the body describes a circle around the flight velocity vector, has particular significance because the steady moment acting on a body in coning motion at low angles of attack can be used to determine the damping-in-pitch derivatives that would be predicted by linear theory. This has been verified experimentally for a slender cone in coning motion in a supersonic stream.[2] At higher angles of attack, however, the measured side moment was observed to depart significantly from the linear theory prediction. Attempts to explain this departure on the basis of the presence and asymmetric disposition of the leeward side vortices had only limited success.[2,3]

This paper reports on an investigation in which numerical techniques were used to study the nonlinear effects of the inviscid flowfield surrounding a body in coning motion. A shock-capturing, finite-difference method developed for the computation of steady, three-dimensional, supersonic flowfields[4,5] is extended to the case of coning motion. Results of computations for slender bodies in coning motion are presented and show good agreement with experiment for angles of attack up to twice the cone half-angle.

Analysis

In the following analysis the center of gravity of the body is considered to move in a straight line path, that is, with no lateral

Presented as Paper 72-27 at the AIAA 10th Aerospace Sciences Meeting, San Diego, Calif., January 17–19, 1972; submitted January 19, 1972; revision received June 5, 1972.

Index categories: Supersonic and Hypersonic Flows; Nonsteady Aerodynamics.

* Research Scientist, Computational Fluid Dynamics Branch. Member AIAA.

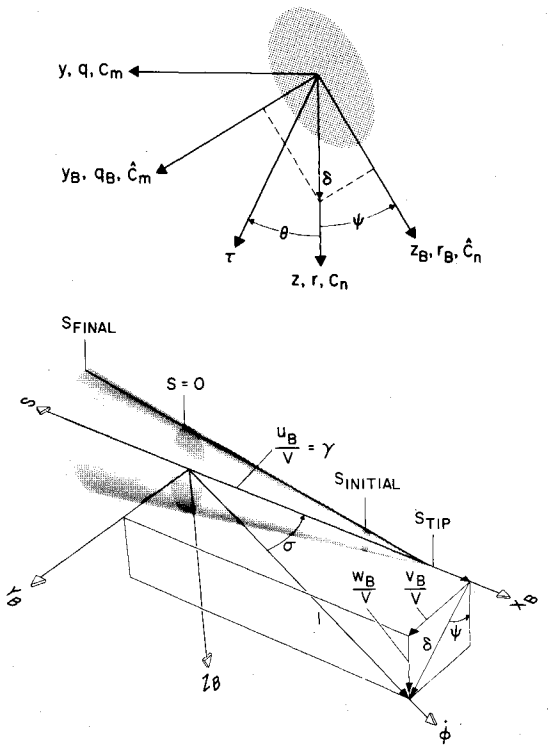

Fig. 1 Axes, angles, and velocity components in the crossflow and resultant angle of attack planes.

or plunging motion, at constant velocity. The application of the results to the case of free flight is straightforward and presented in Ref. 1.

Coordinate Systems

Three coordinate systems having a common origin at the center of gravity will be used (Fig. 1). Axes x_B, y_B, z_B are body-fixed axes, with x_B aligned with a longitudinal axis of the body. The plane formed by y_B, z_B is the crossflow plane illustrated in the top of Fig. 1. The components of the flight velocity vector of magnitude V, resolved along the x_B, y_B, z_B body axes, are u_B, v_B, w_B, respectively. The resultant angle of attack σ is defined by the flight velocity vector and the x_B axis, while the vector with magnitude δ is the projection of the normalized velocity vector in the crossflow plane. Reference to the bottom of Fig. 1, gives

$$\delta = [(v_B/V)^2 + (w_B/V)^2]^{1/2} = \sin\sigma; \quad \gamma = u_B/V = \cos\sigma \tag{1}$$

Axes x_B, y, z will be called the aerodynamic axis system. Axis z lies in the crossflow plane and is alined with the direction of δ; axis y lies in the crossflow plane alined with an axis normal to the direction of δ. The body-fixed axes are oriented relative to the aerodynamic axes by a rotation through the angle ψ about the x_B axis. The components of the angular velocity vector (of the body-fixed axes relative to inertial space) resolved in the aerodynamic axis system, p_B, q, r, are related to those resolved in the body-axis system, p_B, q_B, r_B, through

$$q + ir = e^{i\psi}(q_B + i r_B) \tag{2}$$

Following Ref. 1, w_B/V will be called the angle-of-attack parameter $\hat{\alpha}$, and v_B/V will be called the angle-of-sideslip parameter $\hat{\beta}$. They are related to the standard NASA definitions of angle of attack α and angle of sideslip β through

$$\tan\alpha = w_B/u_B = \hat{\alpha}/\gamma$$
$$\sin\beta = v_B/V = \hat{\beta} \tag{3}$$

and to δ and ψ through

$$\hat{\alpha} + i\hat{\beta} = \delta e^{i\psi} \tag{4}$$

The moment coefficient components measured along the x_B, y_B, z_B body axes are called $\hat{C}_l$, $\hat{C}_m$, $\hat{C}_n$, respectively, while those measured along the x_B, y, z aerodynamic axes are called C_l, C_m, C_n, respectively. Finally, a cylindrical coordinate system, s, τ, θ, with s positive in the negative x_B direction, will be called the computational axis system. The radial coordinate τ lies in planes parallel to the crossflow plane with θ the circumferential angle measured from the z aerodynamic axis (Fig. 1). The angular velocity components in the computational axis system, ω_1, ω_2, ω_3, are related to those in the aerodynamic axis system through

$$\omega_1 = -p_B; \quad \omega_3 + i\omega_2 = e^{i\theta}(q + ir) \tag{5}$$

Coning motion is defined as motion with σ = const, ψ = const, and $\dot{\phi}$ (the coning rate of the longitudinal x_B axis around the flight velocity vector) = const. Under these conditions $p_B = \gamma\dot{\phi}$, $q = 0$, and $r = \delta\dot{\phi}$.

Nonlinear Moment Formulation

In the aerodynamic axis system the nonlinear formulation for the pitching-moment coefficient is[1]

$$C_m(t) = C_m(\infty; \delta(t), \psi(t)) + (\dot{\psi}l/V)\, C_{m_{\dot{\psi}}}(\delta(t), \psi(t)) + (\dot{\sigma}l/V)\, C_{m_{\dot{\sigma}}}(\delta(t), \psi(t)) + (\dot{\phi}l/V)\, C_{m_{\dot{\phi}}}(\infty; \delta(t), \psi(t)) \tag{6}$$

The formulation contains only terms of first order in the rates and is therefore valid only for low reduced frequencies, but the values of δ and ψ may be large. The corresponding formulations for the side-moment and the rolling-moment coefficients are obtained by replacing m by n and l, respectively, in Eq. (6). The term $C_m(\infty; \delta(t), \psi(t))$ is the pitching-moment coefficient that would be measured in steady planar motion with δ and ψ held fixed. The term $C_{m_{\dot{\psi}}}$ is the change in the pitching-moment coefficient due to damping-in-roll motion (small oscillations in ψ about ψ = const with δ = const, $\dot{\phi} = 0$). The term $C_{m_{\dot{\sigma}}}$ is the damping-in-pitch coefficient for planar pitching oscillations (small oscillations in σ about δ = const, with ψ = const, $\dot{\phi} = 0$). The remaining term, $C_{m_{\dot{\phi}}}(\infty; \delta(t), \psi(t))$ is the change in the pitching-moment coefficient due to steady coning motion (ψ = const, δ = const, $\dot{\phi}$ = const). Thus, the complete specification of the moments acting on a body in a general nonplanar motion requires knowledge of moments acting on the body in four characteristic motions: steady angle of attack, damping-in-pitch, damping-in-roll, and coning motion.

One important result of the nonlinear moment formulation[1] is the following relation between moment coefficients measured in the aerodynamic axis system and those measured in the body-fixed axis system

$$C_{n_{\dot{\phi}}}(\infty; \delta, \psi) - \gamma C_{n_{\dot{\psi}}}(\delta, \psi) + \delta C_{m_{\dot{\sigma}}}(\delta, \psi) = \delta\{[\hat{C}_{m_{q_B}}(\infty; \hat{\alpha}, \hat{\beta}) + \gamma\hat{C}_{m_{\hat{\alpha}}}(\hat{\alpha}, \hat{\beta})] + [\hat{C}_{n_{r_B}}(\infty; \hat{\alpha}, \hat{\beta}) - \gamma\hat{C}_{n_{\hat{\beta}}}(\hat{\alpha}, \hat{\beta})]\} \tag{7}$$

The term $C_{n_{\dot{\phi}}}$ is the rate of change with $\dot{\phi}l/V$, evaluated at $\dot{\phi} = 0$, of the side-moment coefficient that would be measured in steady coning motion (ψ = const, δ = const, $\dot{\phi}$ = const), while the term $C_{n_{\dot{\psi}}}$ is the change in the side-moment coefficient due to damping-in-roll motion (small oscillations in ψ about ψ = const, with δ = const, $\dot{\phi} = 0$). The term $(\hat{C}_{m_{q_B}} + \gamma\hat{C}_{m_{\hat{\alpha}}})$ is the planar damping-in-pitch coefficient measured along y_B in the body-fixed axis system for small oscillations in $\hat{\alpha}$ about $\hat{\alpha}$ = const, with $\hat{\beta}$ held fixed at $\hat{\beta}$ = const. Similarly, $(\hat{C}_{n_{r_B}} - \gamma\hat{C}_{n_{\hat{\beta}}})$ is the damping-in-yaw coefficient measured along z_B for small oscillations in $\hat{\beta}$ about $\hat{\beta}$ = const, with $\hat{\alpha}$ = const. Thus, a calculation of $(C_{n_{\dot{\phi}}} - \gamma C_{n_{\dot{\psi}}})$ would be equivalent to a calculation of a combination of the three damping coefficients. The identity is shown in Fig. 2. There are two cases of special interest that lead to simplifications of Eq. (7); when $\psi = 0$ ($\hat{\alpha} = \delta$, $\hat{\beta} = 0$), and when $\psi = \pi/2$ ($\hat{\alpha} = 0$, $\hat{\beta} = \delta$). In the first case $[C_{n_{\dot{\phi}}}(\infty; \delta, 0) - \gamma C_{n_{\dot{\psi}}}(\delta, 0)] = \delta[\hat{C}_{n_{r_B}}(\infty; \hat{\alpha}, 0) - \gamma\hat{C}_{n_{\hat{\beta}}}(\hat{\alpha}, 0)]$, and in the second case $[C_{n_{\dot{\phi}}}(\infty; \delta, \pi/2) - \gamma C_{n_{\dot{\psi}}}(\delta, \pi/2)] = \delta[\hat{C}_{m_{q_B}}(\infty; 0, \hat{\beta}) + \gamma\hat{C}_{m_{\hat{\alpha}}}(0, \hat{\beta})]$. Calculation of $(C_{n_{\dot{\phi}}} - \gamma C_{n_{\dot{\psi}}})$ as $\delta \to 0$ for these cases is seen to be equivalent to calculation of the linear damping-in-yaw and damping-in-pitch coefficients, respectively.

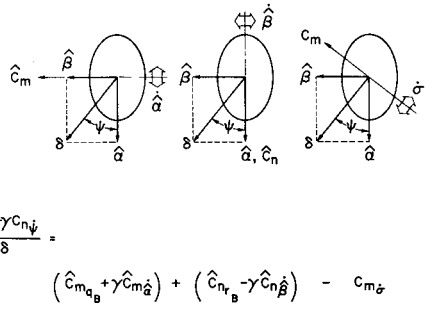

$$\frac{C_{n_{\dot\phi}}-\gamma C_{n_{\dot\psi}}}{\delta} =$$

$$\left(\hat{C}_{m_{q_B}}+\gamma\hat{C}_{m_{\dot\alpha}}\right) + \left(\hat{C}_{n_{r_B}}-\gamma\hat{C}_{n_{\dot\beta}}\right) - C_{m_{\dot\sigma}}$$

Fig. 2 Schematic representation of the equality between $(C_{n_{\dot\phi}} - \gamma C_{n_{\dot\psi}})/\delta$ and the three damping coefficients.

For a body with axial symmetry about the x_B axis ψ can arbitrarily be chosen equal to $\pi/2$ to simplify Eq. (7). Also, in the case of a body of revolution, the only contribution to the damping-in-roll term $C_{n_{\dot\psi}}$ is viscous shear at the body surface. Experimental investigation[2] and a viscous theory[6] have shown this contribution to be negligibly small. Further, an inviscid theory or computation for a body of revolution must give $C_{n_{\dot\psi}} \equiv 0$. Thus, for the body of revolution, calculation of $C_{n_{\dot\phi}}$ alone as $\delta \to 0$ determines the linear damping-in-pitch coefficient. For bodies not possessing axial symmetry about x_B, $C_{n_{\dot\psi}}$ does not necessarily vanish. For short slender bodies of noncircular cross section, however, $C_{n_{\dot\psi}}$ can probably be neglected in comparison with $C_{n_{\dot\phi}}$.

Numerical Method

Recent increases in the speed of digital computers, and the development of computer graphic devices that permit the rapid interpretation of large amounts of data, have stimulated the development and use of highly accurate finite-difference techniques for the solution of fluid dynamics problems. One of these, the noncentered second-order scheme introduced by MacCormack[4] and developed by Kutler and Lomax[5] as a shock-capturing method for the solution of steady three-dimensional inviscid supersonic flowfields has been shown to be both accurate and versatile. The method uses the nonlinear Eulerian gasdynamic equations, and is therefore accurate at hypersonic as well as at supersonic Mach numbers. Results of recent computations of the complex steady flowfield surrounding a typical space shuttle orbiter using the method[7] show excellent agreement with experiment and with other inviscid methods. The advantages of the shock-capturing technique over sharp-shock techniques such as the method of characteristics are twofold. First is its ability to determine the position and strength of the bow shock wave without special computer coding. Second, and more important is its ability to determine the position and strength of embedded shock waves, such as the crossflow shocks which occur on the leeward side of bodies at large angles of attack, within the flowfield.

Method of solution

The nonlinear Eulerian gasdynamic equations are solved for the inviscid flow of a perfect gas about a body in coning motion (δ = const, ψ = const, $\dot\phi$ = const) in a supersonic flow. Under these conditions the flowfield is time invariant with respect to an observer fixed in the s, τ, θ computational axis system. Since the flow is supersonic, the gasdynamic equations are hyperbolic in the s direction. With the flowfield specified at some initial data plane $s = s_{initial}$, the gasdynamic equations are integrated downstream, using the boundary conditions of undisturbed flow ahead of the bow shock wave, and of no flow through the body surface. MacCormack's method is used to integrate the equations from $s_{initial}$ to s_{final} determining the entire flowfield. The forces and moments are obtained from a subsequent integration of the resulting surface pressure distribution. Computations have been performed for conical bodies of circular and elliptical cross section. An approximate initial solution was generated at $s = s_{initial}$ by assuming the flow upstream to be that about a cone at angle of attack and yaw, with a sidewash velocity given by $\dot\phi s_{initial} \sin\sigma$. Details of the method and a discussion of the approximate starting solution are given below.

Computations were performed on an IBM 360/67 computer linked to a cathode-ray tube graphics device. The graphics unit, which possesses man-machine interaction capability, was used to study the flowfield as it developed and to control any numerical instabilities that evolved. Approximately 50 min of computer time was required per case (one angle of attack at one coning rate).

Flow equations

Relative to an observer fixed in the s, τ, θ computational coordinate system, the flowfield surrounding a body in coning motion is time-invariant. In this coordinate system the gasdynamic equations for the steady inviscid flow of a non-heat-conducting perfect gas can be written in conservation-law form as

$$E'_s + F'_\tau + G'_\theta + H' = 0 \tag{8}$$

where, for example, E'_s denotes differentiation of E' with respect to s, and

$$E' = \begin{vmatrix} \rho u \\ p + \rho u^2 \\ \rho uv \\ \rho uw \end{vmatrix} \quad F' = \begin{vmatrix} \rho v \\ \rho uv \\ p + \rho v^2 \\ \rho vw \end{vmatrix} \quad G' = \tfrac{1}{\tau} \begin{vmatrix} \rho w \\ \rho uw \\ \rho vw \\ p + \rho w^2 \end{vmatrix}$$

$$H' = \tfrac{1}{\tau} \begin{vmatrix} \rho v \\ \rho uv + \rho\tau[2(\omega_2 w - \omega_3 v) + \omega_1\omega_2\tau - s(\omega_2^2 + \omega_3^2)] \\ \rho(v^2 - w^2) + \rho\tau[2(\omega_3 u - \omega_1 w) + \omega_2\omega_1 s - \tau(\omega_3^2 + \omega_1^2)] \\ 2\rho vw + \rho\tau[2(\omega_1 v - \omega_2 u) + (\omega_2\tau + \omega_1 s)\omega_3] \end{vmatrix}$$

The components of the total angular velocity $\dot\phi$ in the s, τ, θ directions are respectively, $\omega_1 = -\dot\phi\cos\sigma$, $\omega_2 = \dot\phi\sin\sigma\cos\theta$, $\omega_3 = -\dot\phi\sin\sigma\sin\theta$. Equation (8) represents the continuity and three momentum equations. The terms in H' containing $\omega_1, \omega_2, \omega_3$ are centrifugal and Coriolis force terms that appear because the s, τ, θ computational system is noninertial. For coning motion the energy equation can be written as

$$p = [(\bar\gamma - 1)/2\bar\gamma]\rho[2h_0 + \Phi - (u^2 + v^2 + w^2)] \tag{9}$$

where

$$\Phi = \dot\phi^2[(s\sin\sigma)^2 + s\tau\sin 2\sigma\cos\theta + \tau^2(1 - \sin^2\sigma\cos^2\theta)]$$

Differencing scheme

To facilitate the numerical solution of Eq. (8) the annular region of interest about the body (in the τ, θ plane) is transformed into a rectangular region. Following Ref. 7, the transformed radial independent coordinate μ is chosen to map the region between the body and an outer boundary into the region $0 \le \mu \le 1$. The outer boundary is chosen to lie in the undisturbed flow ahead of the bow shock wave. The transformed circumferential independent coordinate η is chosen to group the circumferential planes more closely in the regions of high flow gradients for the elliptical cones. The transformations are

$$\begin{aligned} &s = s, \quad s_{initial} \le s \le s_{final} \\ &\mu = (\tau - \tau_b)/(\tau_{ob} - \tau_b), \quad 0 \le \mu \le 1 \\ &\eta = \tan^{-1}(BC\tan\theta/A), \quad 0 \le \eta \le 2\pi \end{aligned} \tag{10}$$

where

$\tau_b = \tau_b(\theta, s)$ = value of τ at body surface

$\tau_{ob} = \tau_{ob}(\theta, s)$ = value of τ at outer boundary

A = tangent of the angle subtended by the semimajor axis, $a(s)$, of the elliptical cone, $a(s)/(s - s_{tip})$; B = tangent of the

angle subtended by the semiminor axis, $b(s)$, of the elliptical cone, $b(s)/(s - s_{tip})$; $C = [(1 + A^2)/(1 + B^2)]^{1/2}$. Applying these transformations to Eq. (8) gives

$$E_s + F_\mu + G_\eta + H = 0 \tag{11}$$

where

$$E = E'$$

$$F = (b'\tau_{b_s} + c'\tau_{ob_s})E' + a'F' + (b'\tau_{b_\theta} + c'\tau_{ob_\theta})G'$$

$$G = \sin\eta\cos\eta\left[\frac{B_s}{B(1+B^2)} - \frac{A_s}{A(1+A^2)}\right]E' + \frac{B^2C^2\cos^2\eta + A^2\sin^2\eta}{ABC}G'$$

$$H = H' + \left[(2\sin^2\eta - 1)\left(\frac{B_s}{B(1+B^2)} - \frac{A_s}{A(1+A^2)}\right) - a'(\tau_{b_s} - \tau_{ob_s})\right]E' + \left[\frac{2\sin\eta\cos\eta}{ABC}(B^2C^2 - A^2) - a'(\tau_{b_\theta} - \tau_{ob_\theta})\right]G'$$

$$a' = 1/(\tau_{ob} - \tau_b); \quad b' = (\mu - 1)a'; \quad c' = -\mu a'$$

Here, B_s denotes differentiation of B with respect to s, $\tau_{ob\theta}$ denotes differentiation of τ_{ob} with respect to θ, etc. The rectangular region of interest in the μ,η plane is divided into a rectangular computational grid having 20 equal intervals of magnitude $\Delta\mu$ in the μ direction and 36 equal intervals of magnitude $\Delta\eta$ in the η direction. Thus, $\Delta\mu = 0.05$, and $\Delta\eta = \pi/18$. Applying MacCormack's two step differencing scheme to integrate Eq. (11)

$$\tilde{E}^{n+1}_{j,k} = E^n_{j,k} - \frac{\Delta s}{\Delta\mu}(F^n_{j+1,k} - F^n_{j,k}) - \frac{\Delta s}{\Delta\eta}(G^n_{j,k+1} - G^n_{j,k}) - \Delta s\, H^n_{j,k}$$

$$E^{n+1}_{j,k} = \tfrac{1}{2}\left[E^n_{j,k} + \tilde{E}^{n+1}_{j,k} - \frac{\Delta s}{\Delta\mu}\left(\tilde{F}^{n+1}_{j,k} - \tilde{F}^{n+1}_{j-1,k}\right) - \frac{\Delta s}{\Delta\eta}\left(\tilde{G}^{n+1}_{j,k} - \tilde{G}^{n+1}_{j,k-1}\right) - \Delta s\,\tilde{H}^{n+1}_{j,k}\right] \tag{12}$$

where $\tilde{E}^n_{j,k} = \tilde{E}(n\Delta s, j\Delta\mu, k\Delta\eta)$, the predicted value of E at $n\Delta s$; $E^n_{j,k} = E(n\Delta s, j\Delta\mu, k\Delta\eta)$, the corrected value of E at $n\Delta s$; and $F^n_{j,k} = F(E^n_{j,k})$, $\tilde{F}^n_{j,k} = F(\tilde{E}^n_{j,k})$, etc. The solution is monitored on the graphics device, and the stepsize, Δs, is set as large as is possible without causing the numerical method to become unstable. After each downstream step the flow variables are obtained at each grid point in the μ,η plane from the new values of the vector E and the energy equation as follows

$$E = \begin{vmatrix} \rho u \\ p + \rho u^2 \\ \rho uv \\ \rho uw \end{vmatrix} = \begin{vmatrix} e_1 \\ e_2 \\ e_3 \\ e_4 \end{vmatrix} \tag{13}$$

$$p = \left(\frac{\bar{\gamma} - 1}{2\bar{\gamma}}\right)\rho[2h_0 + \Phi - (u^2 + v^2 + w^2)]$$

The simultaneous solution of Eq. (13) for the flow variables is

$$v = e_3/e_1; \quad w = e_4/e_1$$

$$u = (1/2e_6)[-e_5 + (e_5^2 - 4e_6e_7)^{1/2}]$$

$$\rho = e_1/u; \quad p = [(\bar{\gamma} - 1)/2\bar{\gamma}]\rho[2h_0 + \Phi - (u^2 + v^2 + w^2)] \tag{14}$$

where

$$e_5 = -2\bar{\gamma}e_2/e_1; \quad e_6 = \bar{\gamma} + 1; \quad e_7 = (\bar{\gamma} - 1)[2h_0 + \Phi - (v^2 + w^2)]$$

The positive sign appearing before the radical in Eq. (14) is used because u is supersonic throughout the flowfield. The flow variables are then used to form the conservation-law variables F, G, and H as needed. Thus, given E at some initial data plane $s = s_{initial}$, determination of E at all successive values of s is straightforward.

Boundary conditions

The outer edge, $\mu = 1$, of the computational grid is chosen to lie in the undisturbed freestream ahead of the bow shock. The pressure and density at the outer boundary are fixed at freestream values, and the velocity components are determined from geometrical considerations. At the sides of the computational grid, $\eta = 0$ and $\eta = 2\pi$, a periodic continuation principle is used, that is, $p(0,\mu) = p(2\pi,\mu)$, $\rho(0,\mu) = \rho(2\pi,\mu)$, etc. The tangency boundary condition at the body, $\mu = 0$, is due to a scheme of Abbett[8] and is briefly summarized here. The flow variables are known after the predictor step. In general, the local flow velocity at the body is not tangent to the body. A local two-dimensional Prandtl-Meyer expansion or an isentropic compression is used as needed to turn the flow into the local tangent plane. This satisfies the tangency condition and determines a corrected value of the surface pressure. A corrected value of surface density is then determined, since it is assumed that flow along surface streamlines is isentropic. The magnitude of the corrected flow velocity is then determined from the energy equation, Eq. (9), while its direction is that obtained from satisfying the tangency condition. A more detailed description of the scheme, and a comparison of its abilities with those of other tangency boundary condition schemes, is found in Ref. 7.

Initial solution

An initial solution is generated at $s = s_{initial}$ by assuming the flow upstream to be that around a cone at angle of attack and yaw. Specifically, for the conical body in coning motion (δ = const, ψ = const, $\dot{\phi}$ = const) the initial solution is that of steady planar flow ($\dot{\phi} = 0$) past the body at the same value of δ and ψ, with a uniform sidewash velocity of $\dot{\phi}s_{initial}\sin\sigma$ imposed in the negative y direction. When a cone with apex coincident with that of the conical body is chosen as the outer boundary, corresponding points in successive μ,η planes lie along rays of the conical flowfield. The flowfield is set to freestream values and the equations integrated downstream. When, at corresponding points, no change in the flow variables is detected with further integration downstream, the flow variables are constant along rays, and the conical flow solution has been determined. The conical solution is then scaled to place it at $s = s_{initial}$.

The errors associated with the approximate initial solution should be small, and the assumed flowfield should approach the actual one as the integration proceeds downstream from $s = s_{initial}$. Further, these errors should have only negligible effect on the forces and moments, since the surface area of the body is small near its apex. These errors were assessed by performing a series of computations for one case, letting $s_{initial}$ approach s_{tip}. The forces and moments were unaffected as $s_{initial}$ was varied for values of $(s_{initial} - s_{tip})/(s_{final} - s_{tip})$ less than 0.05. This value was used for the remainder of the cases considered.

Results

10° Circular Cone at Mach Number = 2

A series of computations was performed for a 10° half-angle cone performing coning motion at Mach number = 2.0. The computations were performed for angles of attack ranging from 0° to 25° and for a range of the coning-rate parameter $\dot{\phi}l/V$ from 0 to 0.1. These conditions were chosen to duplicate those of the experiment of Ref. 2. In that experiment a six-component balance mounted on a rotating sting was used to measure the forces and moments acting on the body in coning motion. In addition, the vortex patterns present on the leeward side of the model at high angles of attack were investigated using the vapor screen technique.[9]

Normal-force and pitching-moment coefficients

The normal-force and pitching-moment coefficients are presented in Figs. 3a and 3b, respectively. These coefficients were obtained from computations at fixed angles of attack for various coning rates. At each angle of attack no change in the normal force or the pitching-moment coefficient was obtained as the coning-rate parameter was varied. This result, which agrees

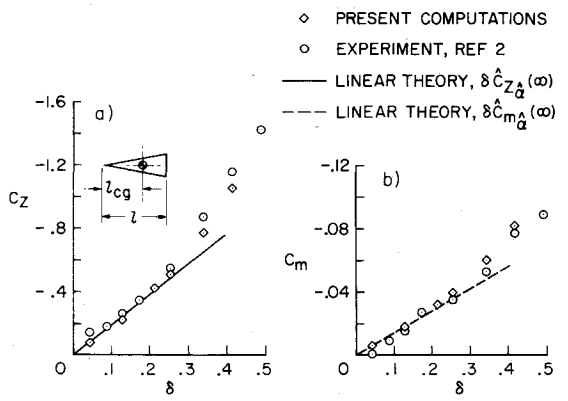

Fig. 3 Normal-force and pitching-moment coefficients for 10° half-angle cone; Mach number = 2.0, lcg/l = 0.61.

with the experimental observations, indicates that $C_{Z_\phi}(\infty;\delta,\psi)$ and $C_{m_\phi}(\infty;\delta,\psi)$, the contributions to the normal-force and pitching-moment coefficients due to coning motion, are negligible.

Also shown in Figs. 3a and 3b are the experimental measurements[2] of the normal-force and pitching-moment coefficients, respectively. The theoretical values[10] of the linear normal-force and pitching-moment coefficients, $\delta\hat{C}_{Z_{\hat{\alpha}}}(\infty)$ and $\delta\hat{C}_{m_{\hat{\alpha}}}(\infty)$, are also presented. At low values of δ the computational results, the experimental measurements, and the linear theory values agree well. As δ increases, the computational results and the experimental measurements become nonlinear functions of δ, and both are greater than the linear theory values. However, the computational results and the experimental measurements remain in good agreement.

Side-force and side-moment coefficients

At fixed angle of attack, the computational results indicate that the side-force and side-moment coefficients C_Y and C_n are linear functions of the coning-rate parameter over the range of $\dot{\phi}$ investigated. This result, which agrees with the experimental findings, demonstrates the adequacy of the moment formulation, Eq. (6), in which only terms linear in $\dot{\phi}$ are retained.

Since C_Y and C_n are linear functions of $\dot{\phi}$, normalizing by the coning-rate parameter gives $C_{Y_{\dot{\phi}}}(\infty;\delta,\psi)$ and $C_{n_{\dot{\phi}}}(\infty;\delta,\psi)$. Computational results for $C_{Y_{\dot{\phi}}}$ and $C_{n_{\dot{\phi}}}$ are presented in Figs. 4a and 4b, respectively, with the experimentally measured values. Also shown in Figs. 4a and 4b are the theoretical values[10] of the linear planar damping-in-pitch derivatives $\delta[\hat{C}_{Z_{q_B}}(\infty)+\gamma\hat{C}_{Z_{\dot{\alpha}}}]$ and $\delta[\hat{C}_{m_{q_B}}(\infty)+\gamma\hat{C}_{m_{\dot{\alpha}}}]$, respectively. At low values of δ, $C_{Y_{\dot{\phi}}}$, and $C_{n_{\dot{\phi}}}$ are linear functions of δ, and there is excellent agreement among the computational results, the experiment measurements, and the linear theory values. As δ increases, the computational results and the experimental measurements become nonlinear functions of δ, and depart significantly from the linear theory results. In contrast, the computational results agree well with the experiment for values of δ up to about 0.35, even as $C_{Y_{\dot{\phi}}}$

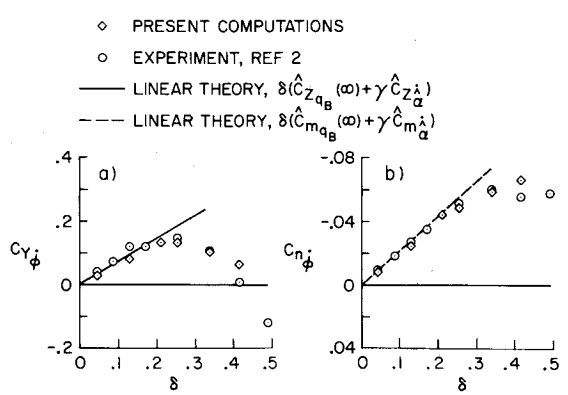

Fig. 4 Side-force and side-moment coefficients on 10° half-angle cone caused by coning motion; Mach number = 2.0, lcg/l = 0.61.

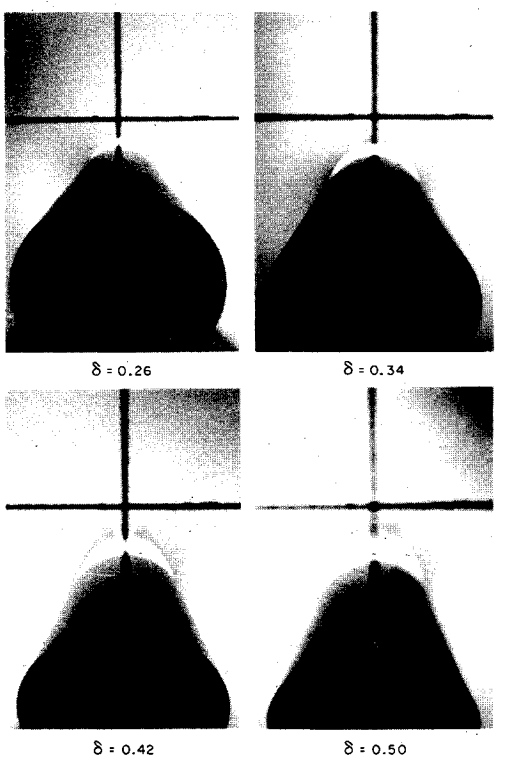

Fig. 5 Typical vapor screen photographs; 10° half-angle cone, Mach number = 2.0.

peaks and then tends toward negative values. As δ increases beyond 0.35 the computational results diverge from the experimental values.

An inviscid flowfield calculation is unable to account for the presence of a vortex pattern on the leeward side induced by viscous-flow separation phenomena. Thus, it is significant (and was unexpected) that the computational results follow the nonlinear behavior of the experimental measurements with increasing values of δ where a leeward side vortex pattern is known to exist. To explain this good agreement an examination was made of the vapor screen studies of the experiment of Ref. 2.

Vapor screen results

Photographs of the leeward side vortex patterns as they appeared in the vapor screen are presented in Fig. 5. The vortex cores are visible as dark spots in a light plane oriented normal to the velocity vector. Distinct vortices are not visible in the vapor screen for values of δ below 0.3. As δ increases, vortices appear but are small and lie close to the body surface. Under these conditions the inviscid flowfield should be a good approximation of the actual one, and the forces and moments derived from the computation should, and do, agree well with the experimental measurements. This indicates that the initial nonlinear behavior of the forces and moments is determined primarily by the inviscid flow. With further increases in δ the vortices gradually grow in size, and presumably in strength, and lie farther from the body. As this growth occurs the inviscid flowfield becomes a poorer approximation of the actual one and the computationally derived forces and moments begin to diverge from those measured experimentally. A more precise determination of the nonlinear behavior of the forces and moments under these conditions would require a method that accounts for the viscous effects. Where the viscous effects are small, nonetheless, the results of the present inviscid computations agree well with experiment and demonstrate the initial nonlinear behavior of the forces and moments.

10° Circular Cone at Mach Number = 10

A computation was performed for a 10° half-angle cone in coning motion at Mach number = 10.0, for an angle of attack

Table 1 Comparison of force and moment coefficients due to coning with corresponding planar coefficients; 10° half-angle cone, Mach number = 10.0, $\alpha = 2.0°$, $\dot{\phi}l/V = 0.2$, $lcg/l = 0.61$

	C_Z $(\delta C_{Z_{\hat{\alpha}}}(\infty))$	C_m $(\delta C_{m_{\hat{\alpha}}}(\infty))$	$C_{Y_{\dot{\phi}}}$ $(\delta[\hat{C}_{Z_{q_B}}(\infty) + \gamma \hat{C}_{Z_{\hat{\alpha}}}])$	$C_{n_{\dot{\phi}}}$ $(\delta[\hat{C}_{m_{q_B}}(\infty) + \gamma \hat{C}_{m_{\hat{\alpha}}}])$
Coning	−0.06717	−0.00588	0.01623	−0.00626
(Planar)[11]	−0.0671	−0.00586	0.0164	−0.00634

of 2° and the coning-rate parameter $\dot{\phi}l/V = 0.2$. At this low angle of attack good agreement is expected between the side-moment coefficient $C_{n_{\dot{\phi}}}$ and the planar damping-in-pitch coefficient $\delta[\hat{C}_{m_{q_B}}(\infty) + \gamma \hat{C}_{m_{\hat{\alpha}}}]$, as predicted by Eq (7). Results of the computation are presented in Table 1 and are compared with the corresponding planar coefficients obtained from the unsteady inviscid flowfield results of Brong.[11] The agreement between the two methods is excellent with the maximum difference seen to be less than 2%. This demonstrates the capability of the present method to give accurate results at hypersonic as well as at supersonic Mach numbers.

Elliptic Cone at Mach Number = 2

Computations were performed for a cone of elliptic cross section in coning motion at Mach number = 1.97. The ratio of the major to minor axes of the cone was 3 : 2, and the base area was equal to that of a 7.75° half-angle circular cone of the same length. The angle of attack was fixed at 4° for values of ψ of 0 and $\pi/2$, and the coning-rate parameter ranged from 0 to 0.15. Computations were also performed for the equivalent circular cone in coning motion.

Normal-force coefficient

The normal-force coefficients obtained from the computations with the bodies in coning motion are presented in Fig. 6a. Again, at fixed angle of attack no change in the normal-force coefficient was obtained as the coning-rate parameter was varied. Also shown in Fig. 6a are experimental values of the normal-force coefficients of these bodies measured at zero coning rate.[12] The good agreement between the computational results and the experimental measurements demonstrates the capability of the method to compute the flowfield about bodies of noncircular cross section. The method can be extended to bodies of arbitrary shape (that is, airplanelike configurations).

Side-moment coefficient

Computed values of the side-moment coefficient $C_{n_{\dot{\phi}}}(\infty; \delta, \psi)$ are presented in Fig. 6b. Also shown is the theoretical value[10] of the linear planar damping-in-pitch derivative $\delta[\hat{C}_{m_{q_B}}(\infty) + \gamma \hat{C}_{m_{\hat{\alpha}}}]$ for the equivalent circular cone. As before, for the circular cone $C_{n_{\dot{\psi}}} \equiv 0$ and there is good agreement between the computed value of $C_{n_{\dot{\phi}}}$ and the linear damping-in-pitch derivative, as predicted by Eq. (7). For the elliptic cone, $C_{n_{\dot{\psi}}}$ does not vanish

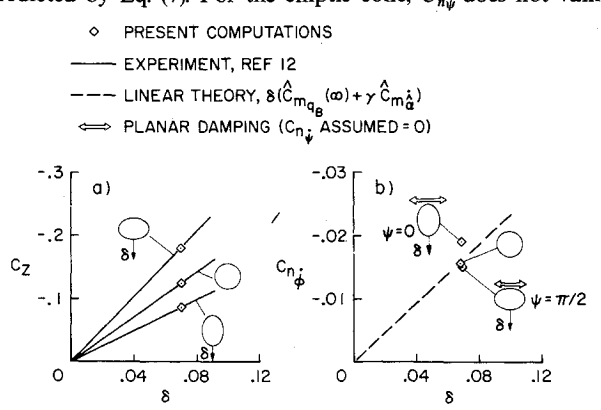

Fig. 6 Normal-force and side-moment coefficients on elliptic cones caused by coning motion; Mach number = 1.97, $lcg/l = 0.61$.

but can probably be neglected in comparison with $C_{n_{\dot{\phi}}}$. Under these conditions $C_{n_{\dot{\phi}}}(\infty; \delta, \pi/2) = \delta[\hat{C}_{m_{q_B}}(\infty) + \gamma \hat{C}_{m_{\hat{\alpha}}}]$ and $C_{n_{\dot{\phi}}}(\infty; \delta, 0) = \delta[\hat{C}_{n_{r_B}}(\infty) - \gamma \hat{C}_{n_{\hat{\beta}}}]$. These are the planar damping coefficients for oscillations in the directions indicated by the double-headed arrows in Fig. 6b. The computational results confirm the expectation that oscillations parallel to the major axis of the elliptical cone should be less strongly damped than those parallel to the minor axis.

Conclusions

A numerical method for computing the steady, inviscid flowfield surrounding a body performing coning motion in a supersonic flow has been presented. The method permits the accurate determination of the aerodynamic moment due to coning, one of the four component motions characterizing an arbitrary nonplanar motion. Moments computed at supersonic and hypersonic Mach numbers for circular cones at low angle of attack confirm the relation between the side moment acting in coning motion and the planar damping-in-pitch given by the linear theory.

Computational results for the moments on a circular cone at higher angles of attack showed significant departures from the linear theory values, but agreed well with experimental measurements within the range of variables investigated. This indicates that the initial nonlinear behavior of the aerodynamic moment is determined primarily by the inviscid flow, with the effects of the leeward-side vortex pattern induced by viscous phenomena becoming important only with further increases in the angle of attack.

References

[1] Tobak, M. and Schiff, L. B., "A Nonlinear Aerodynamic Moment Formulation and Its Implications for Dynamic Stability Testing," AIAA Paper 71-275, 1971, Albuquerque, N. Mex.

[2] Schiff, L. B. and Tobak, M., "Results from a New Wind-Tunnel Apparatus for Studying Coning and Spinning Motions of Bodies of Revolution," *AIAA Journal*, Vol. 8, No. 11, Nov. 1970, pp. 1953–1957.

[3] Kuhn, G. D., Spangler, S. B., and Nielsen, J. N., "Theoretical Analysis of Vortex Shedding from Bodies of Revolution in Coning Motion," *AIAA Journal*, Vol. 9, No. 5, May 1971, pp. 784–790.

[4] Mac Cormack, R. W., "The Effect of Viscosity in Hypervelocity Impact Cratering," AIAA Paper 69-364, Cincinnati, Ohio, 1969.

[5] Kutler, P. and Lomax, H., "Shock-Capturing, Finite-Difference Approach to Supersonic Flows," *Journal of Spacecraft and Rockets*, Vol. 8, No. 12, Dec. 1971, pp. 1175–1182.

[6] Sedney, R., "Laminar Boundary Layer on a Spinning Cone at Small Angles of Attack in a Supersonic Flow," *Journal of the Aeronautical Sciences*, Vol. 24, No. 6, June 1957, pp. 430–436.

[7] Kutler, P., Lomax, H., and Warming, R. F., "Computation of Space Shuttle Flow Fields Using Noncentered Finite Difference Schemes," AIAA Paper 72-193, San Diego, Calif., 1972.

[8] Abbett, M. J., "Boundary Condition Computational Procedures for Inviscid Supersonic Steady Flow Field Calculations," Rept. 71-41, Nov. 1971, Aerotherm Corp., Mountain View, Calif.

[9] Allen, H. J. and Perkins, E. W., "A Study of Effects of Viscosity on Flow Over Slender Inclined Bodies of Revolution," Rept. 1048, 1951, NACA.

[10] Tobak, M. and Wehrend, W. R., "Stability Derivatives of Cones at Supersonic Speeds," TN 3788, 1956, NACA.

[11] Brong, E. A., "The Unsteady Flow Field About a Right Circular Cone in Unsteady Flight," FDL-TDR-64-148, Jan. 1967, Flight Dynamics Lab., Wright-Patterson Air Force Base, Ohio.

[12] Jorgenson, L. H., "Elliptic Cones Alone and With Wings at Supersonic Speeds," TN 4045, 1957, NACA.